Applied Acoustics 71 (2010) 743–753

Contents lists available at ScienceDirect

Applied Acoustics

journal homepage: www.elsevier.com/locate/apacoust

Numerical treatment of acoustic problems with the smoothed finite element method

L.Y. Yao *, D.J. Yu, X.Y. Cui, X.G. Zang

State Key Laboratory of Advanced Design and Manufacturing for Vehicle Body, Hunan University, Changsha 410082, PR China

ARTICLE INFO

Article history:
Received 29 August 2009
Received in revised form 24 March 2010
Accepted 24 March 2010
Available online 20 April 2010

Keywords:
Smoothed finite element method
Finite element method
Acoustic analysis
Nodal irregularity

ABSTRACT

We incorporated a cell-wise acoustic pressure gradient smoothing operation into the standard compatible finite element method and extended the smoothed finite element method (SFEM) for 2D acoustic problems. This enhancement was especially useful for dealing with the problem of an arbitrary shape with violent distortion elements. In this method, the domain integrals that involve shape function gradients can be converted into boundary integrals that involve only shape functions. Restrictions on the shape elements can be removed, and the problem domain can be discretized in more flexible ways. Numerical results showed that the proposed method achieved more accurate results and higher convergence rates than the corresponding finite element methods, even for violently distorted meshes. The most promising feature of SFEM is its insensitivity to mesh distortion. The superiority of the method is remarkable, especially when solving problems that have high wave numbers. Hence, SFEM can be beneficially applied in solving two-dimensional acoustic problems with severely distorted elements, which, in practice, have more foreground than regularity mesh.

1. Introduction

In the past decades, there has been an increasing interest in the simulation of noise, either to satisfy more and more stringent national and international standards or to improve the comfort of end-users. The numerical simulation of elastic and acoustic wave propagation, addressed by the Helmholtz equation, is a field in which intense developments are taking place. There is extensive interest in the search for simple, efficient, and accurate numerical methods that are applicable to acoustic problems. Many researchers have studied many different numerical methods in order to improve the solution of acoustic problems, such as the finite element method (FEM) [1–5] and the boundary element method (BEM) [6]. There are also several other numerical methods that have been used to solve acoustic problems. Harari et al. [7] investigated the stabilized finite element method and appended a stability term that contains gradient to the basic Galerkin formulation. High order approximation, such as the spectral element shape functions proposed by Petersen [8], can lead to improve the accuracy of the assessment of interior acoustic problems.

A well-known problem associated with the use of FEM for the Helmholtz equation is the loss of ellipticity as the wave number increases [9]. This leads to the "pollution effect", especially with high wave numbers, unless a finer mesh is provided. The accuracy of conventional mesh-based methods for solving acoustic problems depends significantly on, for example, the quality of the mesh and element distortion. As element distortion becomes more severe, the "pollution effect" associated with high wave numbers also gets larger. Mesh-free methods developed in the 1990s, have several advantages over classical mesh-based methods. One of the major objectives of the recent development of the mesh-free method was to avoid problems related to element distortion encountered in FEM. Therefore, the pre-processing work for mesh-free methods takes less manpower than FEM, even with distorted mesh. Several researchers have investigated the application of the mesh-free method for dealing with acoustic problems using the Moving Least Square Method (MLSM) [10] and the improved Element-Free Galerkin Method (I-EFGM) [11], which proved that the mesh-free method is more accurate. Kireeva et al. [12] presented the coupling of the Element-Free Galerkin method with a modified conjugated infinite element for acoustic radiation problems in infinite domains.

Although the mesh-free method has good accuracy and a high convergence speed, the complex field approximation inevitably increases the computational cost. In order to overcome this problem, Liu et al. [13,14] recently proposed SFEM by incorporating the strain smoothing operation with the standard finite element techniques. The SFEM shows many superior features over the standard FEM in solving numerical problems with severely distorted elements, and several researchers have investigated the application of SFEM in mechanics problems. A quadrilateral element with

* Corresponding author. Tel.: +86 13467505078.
E-mail address: 19831022y@163.com (L.Y. Yao).

0003-682X/$ - see front matter © 2010 Elsevier Ltd. All rights reserved.
doi:10.1016/j.apacoust.2010.03.006

smoothed curvatures for Mindlin-Reissner plates was proposed by Nguyen-Xuan [15], and, similarly, Nguyen-Thanh [16] proposed such an element for the shell. Cui et al. [17] used SFEM to analyze the linear and geometrically non-linear problems of plates and shells using bi-linear, quadrilateral elements and found that SFEM provided very stable and accurate results compared with the standard FEM techniques. Dai and Liu [18] extended SFEM to the free and forced analysis of two-dimensional dynamic problems.

Based on this previous research, we used SFEM for the acoustic field by coupling acoustic pressure gradient smoothing operation with standard acoustic finite element techniques. For SFEM, the Galerkin weak form and the mesh are used just as they are in FEM. The element is further subdivided into several smoothing cells (SCs), and the cell-wise acoustic pressure gradient smoothing operation is presented in each acoustic element. Then, the smoothed gradients of the acoustic pressure are used for computing the acoustic stiffness matrix. Numerical studies have demonstrated that the acoustic SFEM produces more accurate results and has a higher convergence rate without increasing the computational cost, especially for highly distorted meshes or high wave numbers. The performance of the SFEM for acoustic problems is vastly superior to that of the standard FEM.

The paper is outlined as follows. In Section 2, the Helmholtz wave propagation theory is briefly described. In Section 3, we present the idea and formulation of the acoustic SFEM. In Section 4, SFEM applied to an acoustic problem is presented and compared with the standard FEM in terms of accuracy and convergence. In Section 5, numerical examples, such as the acoustic square domain model, a car passenger acoustic cavity model, and a micro-car passenger acoustic cavity model, are analyzed using both FEM and SFEM, and the effects of nodal irregularity are emphasized. Section 6 contains concluding remarks.

2. Acoustic wave propagation

Based on acoustic theory, the acoustic pressure p is complex-valued in the frequency domain and satisfies the Helmholtz equation given by:

$$\nabla^2 p + k^2 p = 0 \tag{1}$$

where ∇^2 denotes the Laplace operator, and $\boldsymbol{k}$ is the wave number defined as the ratio of angular frequency ω and the speed of sound c:

$$k = \frac{w}{c} \tag{2}$$

The gradient of acoustic pressure p is linked to the velocity v by the equation of motion, which can be written as:

$$\nabla p + j\rho\omega v = 0 \tag{3}$$

where $j = \sqrt{-1}$, and ρ denotes the density of the fluid.

For interior acoustic problems, e.g., an acoustic domain Ω bounded by Γ, there are three sets of initial boundary conditions:

(1) The Dirichlet condition:

$$p = p_D \text{ on } \Gamma_D \tag{4}$$

(2) The Neumann condition:

$$\nabla p \cdot n = -j\rho\omega v_n \text{ on } \Gamma_n \tag{5}$$

(3) The Robin condition:

$$\nabla p \cdot n = -j\rho\omega A_n p \text{ on } \Gamma_x \tag{6}$$

where the normal component of the velocity v_n stands for the excitation by the vibrating panels on condition Γ_n, n is the exterior unit normal vector, and A_n is the admittance coefficient that models the structural damping of the condition Γ_x.

3. The idea and formulation of the acoustic SFEM

This section presents the formulation of SFEM for 2D acoustic problems. Considering an acoustic domain Ω bounded by Γ, the standard Galerkin weak form can be expressed as follows:

$$\int_\Omega w(\Delta p + k^2 p)\mathrm{d}\Omega = 0 \tag{7}$$

where w is a test function. Using Green's formulation and integration by parts, we can obtain:

$$-\int_\Omega \nabla w \cdot \nabla p\,\mathrm{d}\Omega + k^2 \int_\Omega w \cdot p\,\mathrm{d}\Omega + \int_\Gamma w(\nabla p \cdot n)\,\mathrm{d}\Gamma = 0 \tag{8}$$

Substituting Eqs. (4)–(6) into Eq. (8) yields:

$$-\int_\Omega \nabla w \cdot \nabla p\,\mathrm{d}\Omega + k^2 \int_\Omega w \cdot p\,\mathrm{d}\Omega - i\rho\omega \int_{\Gamma_n} w \cdot v_n\,\mathrm{d}\Gamma_n - i\rho\omega A_n \int_{\Gamma_x} w \cdot p\,\mathrm{d}\Gamma_x = 0 \tag{9}$$

In this method, the acoustic domain discretization is based on quadrilateral elements that are the same as those in FEM. The acoustic domain is discretized into N_e quadrilateral elements with N_d nodes. Each element domain Ω is divided into smoothing cells (SCs), such that $\Omega_1 \cup \Omega_2 \cup \ldots \Omega_{SC} = \Omega$ and $\Omega_1 \cap \Omega_2 \cap \ldots \Omega_{SC} = \varnothing$. These smoothing cells (SCs) are shown in Fig. 1. An acoustic gradient smoothing operation is implemented over each smoothing cell, and integration is performed based on the SCs. When choosing a constant smoothing function, area integration over the cell becomes line integration along its boundaries, and no gradient of shape functions is involved in computing the acoustic gradients or in forming the stiffness matrix.

The acoustic pressure at any point in the acoustic domain is interpolated using the element shape functions, which are created in the same way by the linear standard FEM. The pressure can be written as:

$$p(\mathbf{x}) = \sum_{I=1}^{N_p} N_I p_I \tag{10}$$

where N_I is shape function, N_p is the number of the nodal variables of the element, and p_I is a set of nodal values for the pressure field.

A smoothing operation is performed on the gradient of acoustic pressure for each smoothing cell in an element. With the relationship between the gradient of acoustic pressure and velocity in Eq. (3), the smoothing operation is performed on the velocity. The smoothing velocity $\bar{\mathbf{v}}_\mathbf{C}(\mathbf{x})$ in the smoothing domain Ω_C can be written as:

$$\bar{\mathbf{v}}_\mathbf{C}(\mathbf{x}) = \int_{\Omega_\mathbf{C}} \mathbf{v}(\mathbf{x})\mathbf{H}(\mathbf{x})\mathbf{d}\Omega \tag{11}$$

where $\mathbf{v}(\mathbf{x})$ is the compatible velocity:

$$\mathbf{v}(\mathbf{x}) = -\frac{1}{j\rho\omega}\nabla p(\mathbf{x}) \tag{12}$$

and $H(x)$ is a given smoothing function that satisfies at least the unity property:

$$\int_{\Omega_C} H(\mathbf{x})d\Omega = 1 \tag{13}$$

Substituting Eqs. (10) and (12) into Eq. (11) and applying Green's theorem, the smoothing velocity can be expressed as:

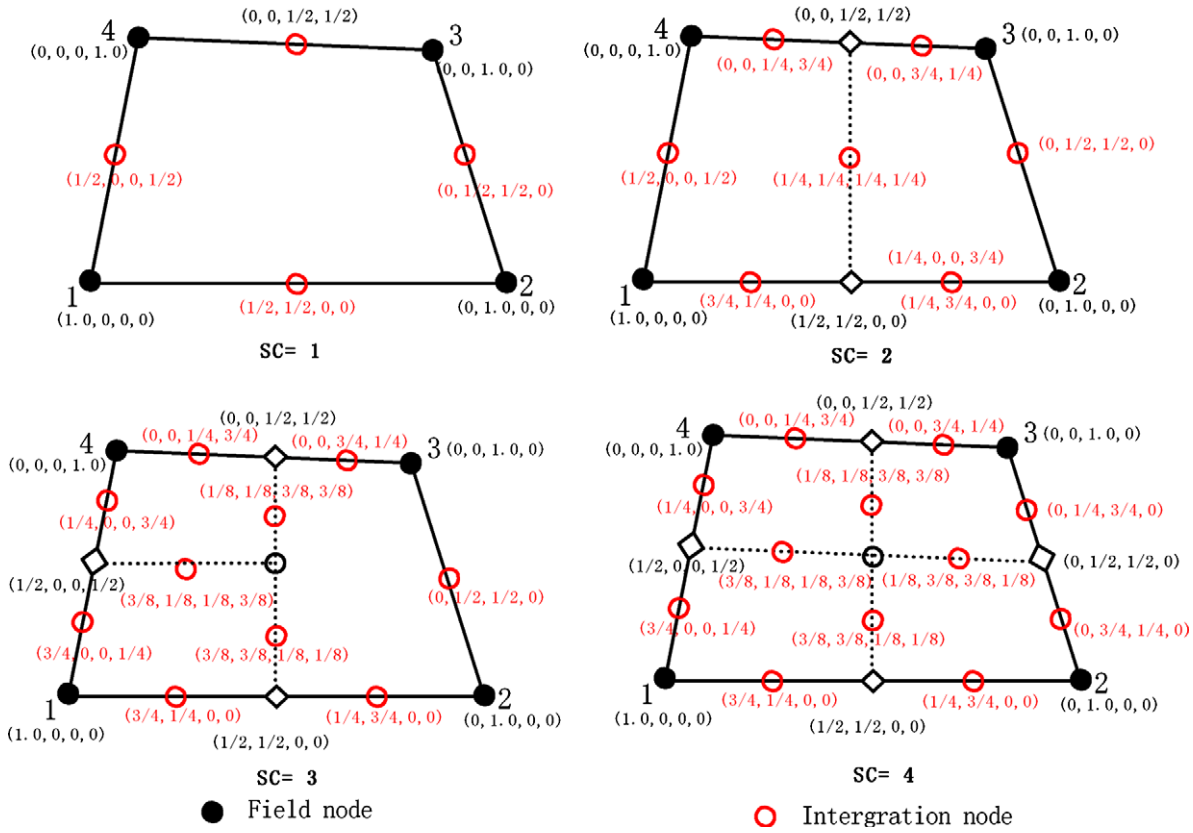

Fig. 1. Subdivision of smoothing cells and the values of shape functions.

$$\overline{\mathbf{v}}_{\mathbf{C}}(\mathbf{x}) = -\frac{\mathbf{1}}{\mathbf{j}\rho\omega}\int_{\Omega_{\mathbf{C}}} \nabla\mathbf{p}(\mathbf{x})\mathbf{H}(\mathbf{x})\mathbf{d}\Omega = -\frac{\mathbf{1}}{\mathbf{j}\rho\omega}\int_{\Gamma_{\mathbf{C}}} \mathbf{p}(\mathbf{x})\mathbf{n}(\mathbf{x})\mathbf{H}(\mathbf{x})\mathbf{d}\Gamma \tag{14}$$

In this paper, we use the constant smoothing function defined as:

$$H(\mathbf{x}) = \begin{cases} 1/A_C & \mathbf{x} \in \Omega_C \\ 0 & \mathbf{x} \notin \Omega_C \end{cases} \tag{15}$$

where $A_C = \int_{\Omega_C} \mathrm{d}\Omega$ is the area of the smoothing domain.

Substituting Eq. (15) into Eq. (14), we obtain the smoothed velocity in terms of acoustic pressure:

$$\overline{\mathbf{v}}_{\mathbf{C}}(\mathbf{x}) = -\frac{\mathbf{1}}{\mathbf{j}\rho\omega}\int_{\Gamma_{\mathbf{C}}} \mathbf{p}(\mathbf{x})\mathbf{n}(\mathbf{x})\mathbf{H}(\mathbf{x})\mathbf{d}\Omega = -\frac{\mathbf{1}}{\mathbf{j}\rho\omega\mathbf{A}_{\mathbf{C}}}\int_{\Gamma_{\mathbf{C}}} \mathbf{p}(\mathbf{x})\mathbf{n}(\mathbf{x})\mathbf{d}\Gamma \tag{16}$$

where Γ_C is the boundary of the smoothed cell, and $\mathbf{n}(\mathbf{x})$ is the outward normal vector matrix on the boundary Γ_C. Note that the area integration becomes line integration along the edges of smoothing cell in Eq. (16).

Substituting Eq. (10) into Eq. (16), the smoothed velocity and acoustic gradient can be obtained:

$$\overline{\mathbf{v}}_{\mathbf{C}}(\mathbf{x}) = -\frac{\mathbf{1}}{\mathbf{j}\rho\omega}\sum_{\mathbf{I}=\mathbf{1}}^{\mathbf{N_I}} \overline{\mathbf{B}}_{\mathbf{I}}(\mathbf{x})\mathbf{p}_{\mathbf{I}} \tag{17}$$

$$\overline{\nabla} p(\mathbf{x}) = \sum_{I=1}^{N_I} \overline{\mathbf{B}}_{\mathbf{I}}(\mathbf{x})\mathbf{p}_{\mathbf{I}} \tag{18}$$

where $\overline{\mathbf{B}}_{\mathbf{I}}$ is the smoothed acoustic gradient matrix in the smoothing cells and is defined as:

$$\overline{\mathbf{B}}_{\mathbf{I}}(\mathbf{x}) = \begin{bmatrix} \bar{b}_{I1} & \bar{b}_{I2} \end{bmatrix}^{\mathbf{T}} \tag{19}$$

in which

$$\bar{b}_{Id} = \frac{1}{A_C}\int_{\Gamma_C} N_I(\mathbf{x}) n_d(\mathbf{x})\mathrm{d}\Gamma \quad d = 1,2 \tag{20}$$

If one Gaussian point is used for line integration along each segment of boundary Γ_C of Ω_C, Eq. (20) can be transformed into its algebraic form:

$$\bar{b}_{Id} = \sum_{I=1}^{N_1} \frac{1}{A_C} N_I(\mathbf{x}_I^{GP}) n_{Id}^C l_I^C \quad (d = 1,2) \tag{21}$$

where N_1 is the number of boundary segments, and $\mathbf{x}_I^{GP}$ is the midpoint (Gaussian point) of the boundary segment of Γ_C, whose length and outward unit normal are denoted as n_I^C and l_I^C, respectively.

Now, the smoothed acoustic gradient is implemented in the Galerkin weak form, and the smoothed weak form is obtained as follows:

$$-\int_\Omega \overline{\nabla} w \cdot \overline{\nabla} p\, d\Omega + k^2 \int_\Omega w \cdot p\, d\Omega - i\rho\omega \int_{\Gamma_n} w \cdot v_n\, d\Gamma_n - i\rho\omega A_n \int_{\Gamma_x} w \cdot p\, d\Gamma_x = 0 \tag{22}$$

Substituting Eqs. (10) and (18) into Eq. (22), the equations over the entire domain are discretized, resulting in the following matrix form:

$$[\overline{\mathbf{K}} - \mathbf{k}^2\mathbf{M} + \mathbf{i}\rho\mathbf{ckC}]\{\mathbf{P}\} = \{\mathbf{F}\} \tag{23}$$

where the element smoothed acoustic stiffness matrix $\overline{\mathbf{K}}$ is expressed as:

$$\overline{\mathbf{K}} = \sum_{\mathbf{C}=\mathbf{1}}^{\mathbf{SC}} \overline{\mathbf{K}}^{\mathbf{C}} \tag{24}$$

The summation represents an assembly process as is done in FEM, SC is the total number of the smoothing cells within the element, and the $\overline{\mathbf{K}}^{\mathbf{C}}$ is the stiffness matrix associated with the Cth smoothing cell, given as:

$$\overline{\mathbf{K}}^{\mathbf{C}} = \int_{\Omega_{\mathbf{C}}} \overline{\mathbf{B}}_{\mathbf{I}}^{\mathbf{T}} \overline{\mathbf{B}}_{\mathbf{I}} \, \mathbf{d}\Omega \tag{25}$$

Matrix **C** is the acoustic damping matrix, which is given by:

$$\mathbf{C} = \int_{\Gamma_3} \mathbf{N}^{\mathrm{T}} \mathbf{N} A_n \, \mathrm{d}\Omega \tag{26}$$

M is the acoustic mass matrix:

$$\mathbf{M} = \int_{\Omega} \mathbf{N}^{\mathrm{T}} \mathbf{N} \, \mathrm{d}\Omega \tag{27}$$

The vector of the nodal acoustic forces **F** is

$$\mathbf{F} = -i\rho ck \int_{\Gamma_2} \mathbf{N}^{\mathrm{T}} v_n \, \mathrm{d}\Omega \tag{28}$$

and **P** is the nodal acoustic pressure in the domain:

$$\{\mathbf{P}\}^T = \{p_1, p_2, \ldots, p_n\} \tag{29}$$

It is obvious that the smoothed acoustic gradient matrix integration can be solved easily and efficiently; area integrations over the cell become line integrations along the cell boundaries, and no gradient of shape functions is involved in computing the field gradients or in forming the smoothed stiffness matrix. Hence, highly distorted elements can be used, and very simple shape functions can be utilized at Gauss points on the edges of the smoothing cell. In the present method, a very simple way to construct shape functions is recommended, as shown in Fig. 1. The values of the shape functions at the integration nodes are determined based on the linear interpolation of shape functions along the boundaries of the element or the smoothing cells [18].

A study conducted by Liu et al. [13] showed that, if SC = 1, the SFEM solution is proven to be 'variationally consistent,' and it has the same properties as FEM when reduced integration is used. If SC approaches infinity, the SFEM solution will approach the solution of the standard displacement compatible FEM model. If SC is a finite number larger than 1, the SFEM solutions are 'energy consistent' rather than 'variationally consistent,' and the value of SC will change continuously from the solution of SFEM for which SC = 1 to the solution of SFEM for which SC approaches infinity. It is suggested that there exists an optimal number of SCs, such that the SFEM solution is closest to the exact solution. Experience indicates that the optimal number of SC is 3 or 4 for acoustic problems.

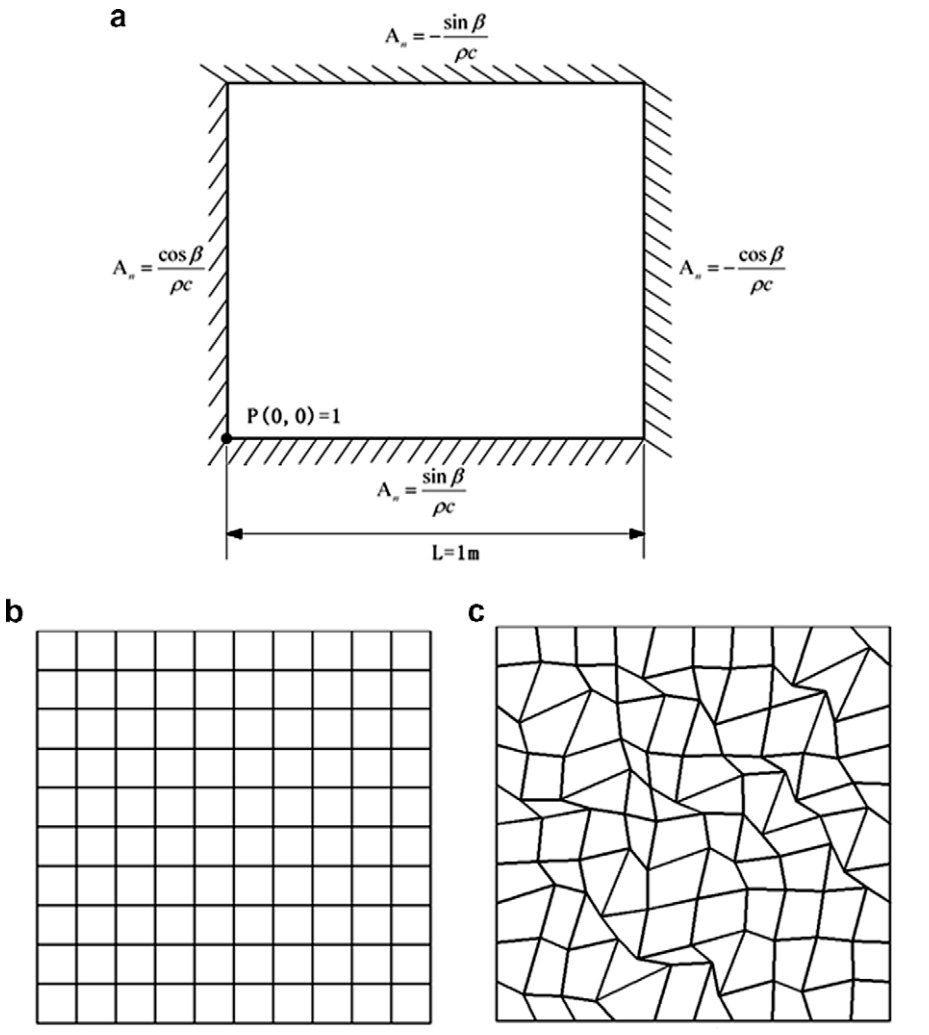

Fig. 2. (a) The 2D acoustic square domain problem, (b) regular mesh, (c) irregular mesh.

4. Numerical tests

4.1. Pollution effect

Consider the standard finite element solution p^h and define the discretization error in the H^1 semi-norm:

$$|p-p^h|_1^2 = \int_\Omega (\tilde{v}^{exact} - v^h)^t (v^{exact} - v^h) d\Omega \tag{30}$$

where $\tilde{v}$ is the complex conjugate of velocity v, the superscript *exact* denotes the *exact* solutions, and h denotes a numerical solution obtained using a numerical method, including the present SFEM and FEM code with the same mesh.

Ihlenburg and Babuska [19,20] proved that the error contains two terms, i.e., the interpolation error and the pollution error. The interpolation error defines the difference between the exact wave and its interpolant, and the pollution error defines the difference between the interpolant and the finite element wave. The general estimate for the relative error in H^1 semi-norm for the *hp* version of the finite element method [21] is:

$$e = \frac{|p-p^h|_1}{|p|_1} = \frac{\int_\Omega (v-v^h)^t (v-v^h) d\Omega}{\int_\Omega v^2 d\Omega} \leqslant C_1' \left(\frac{kh}{n}\right)^p + C_2' k \left(\frac{kh}{n}\right)^{2n} \tag{31}$$

where C_1 and C_2 are constants that are independent of the parameters k and h, and n is the degree of the polynomial approximation of the numerical method. With the linear interpolation ($n = 1$) discussed here, the relative error can be expressed by:

$$e \leqslant C_1 kh + C_2 k^3 h^2 \tag{32}$$

4.2. The acoustic square domain problem

This two-dimensional problem considers a square domain, and L is the length of its side. Robin boundary conditions are defined on all four sides as shown in Fig. 2a. This example was modeled by Bouillard and Suleau [10]. Regular and irregular meshes of 10×10 elements were studied, as shown in Fig. 2b and c.

The pressure is prescribed at one of the corners. The strong form of this problem is expressed, in its non-dimensional form, by the Helmholtz equation:

$$\frac{\partial^2 p}{\partial \xi^2} + \frac{\partial^2 p}{\partial \eta^2} + \kappa^2 p = 0 \quad \text{in } \Omega\ (0 \leqslant \xi \leqslant 1; 0 \leqslant \eta \leqslant 1) \tag{33}$$

with the Dirichlet boundary condition:

$$p(0,0) = 1 \tag{34}$$

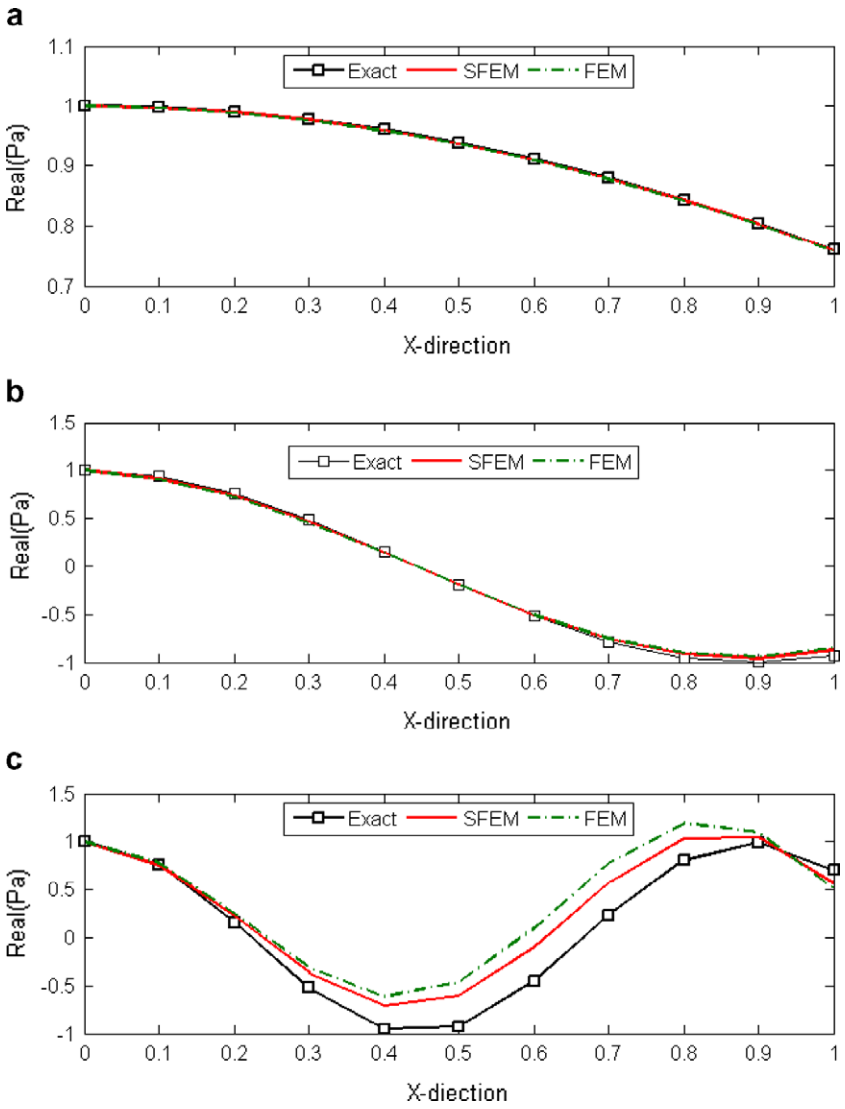

Fig. 3. Spatial distribution of real part of the pressure: (a) $\boldsymbol{k} = 1$, (b) $\boldsymbol{k} = 5$, (c) $\boldsymbol{k} = 10$.

and the Robin boundary conditions:

$$\begin{cases} -\frac{\partial p}{\partial \xi} + jkp\cos\beta = 0 & \text{on} \quad (\xi = 0, \eta) \\ \frac{\partial p}{\partial \xi} - jkp\cos\beta = 0 & \text{on} \quad (\xi = 1, \eta) \\ -\frac{\partial p}{\partial \eta} + jkp\sin\beta = 0 & \text{on} \quad (\xi, \eta = 0) \\ \frac{\partial p}{\partial \eta} + jkp\sin\beta = 0 & \text{on} \quad (\xi, \eta = 1) \end{cases} \tag{35}$$

This two-dimensional problem corresponds to a plane wave propagating along a direction inclined with an angle β on axis x. The analytical solution is:

$$p = \cos[\kappa(\xi\cos\beta + \eta\sin\beta)] + j\sin[\kappa(\xi\cos\beta + \eta\sin\beta)] \tag{36}$$

Three different values of wave numbers ($\boldsymbol{k} = 1$, $\boldsymbol{k} = 5$, $\boldsymbol{k} = 10$) for this problem have been studied for a value of $\beta = 45°$. Fig. 3a–c plot the acoustic pressure distributions separately along the x-axis boundary line using SFEM. For comparison, exact and linear FEM solutions are also plotted. The results of the exact solution, FEM solution, and SFEM solution are presented in Fig. 3.

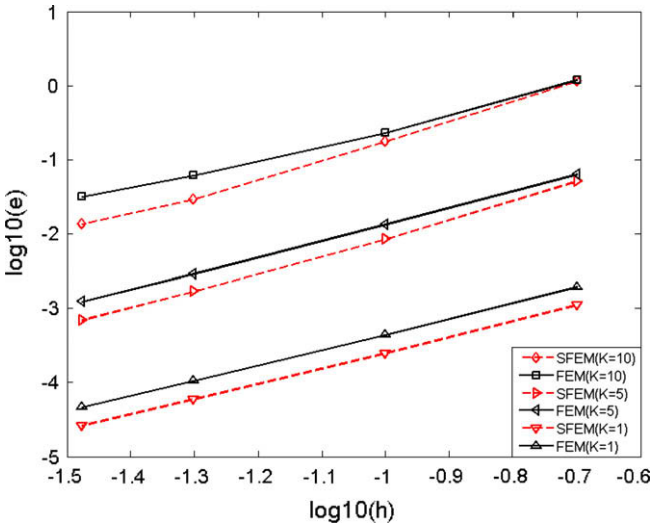

Fig. 4. Comparison of accuracy and convergence property between SFEM and linear FEM.

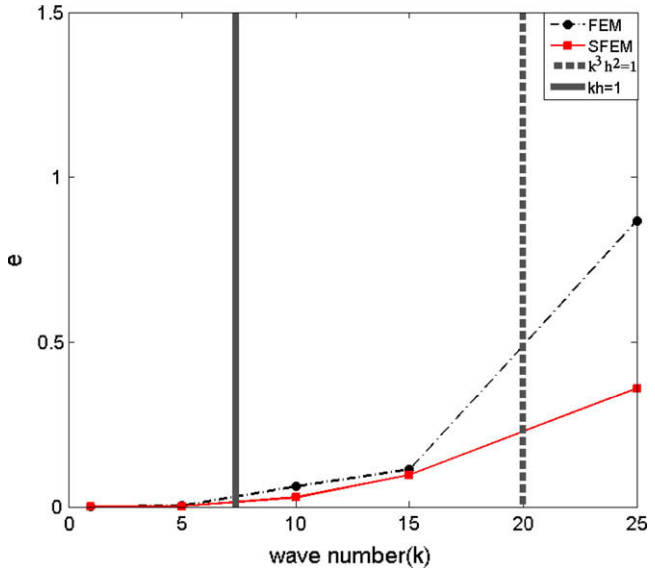

Fig. 5. The relation between relative error and wave number.

It can be seen from Fig. 3 that:

(1) For low wave number problems, FEM and SFEM are in good agreement with the exact solution.
(2) For high wave number problems, the errors of FEM and SFEM increased as wave number increased, but the results obtained from SFEM for acoustic pressure were slightly more accurate than those obtained from the linear FEM.

4.3. Accuracy and convergence

The accuracy and convergence properties of SFEM were investigated at three different wave number values ($\boldsymbol{k} = 1$, $\boldsymbol{k} = 5$, $\boldsymbol{k} = 10$) using four types of uniformly distributed nodes (36, 121, 441, and 961 nodes). The results obtained from the linear FEM and SFEM in terms of the relative error are plotted in Fig. 4, which shows that SFEM can generally achieve better accuracy and a higher convergence rate than FEM. As frequency increases, the errors associated with both SFEM and FEM get larger, but the relative error with SFEM was smaller than the relative error of FEM. These results clearly showed that the error associated with the SFEM solution was slightly less sensitive to frequency increases than the FEM solution.

The sensitivity of the relative error to wave number $\boldsymbol{k}$ was also investigated with a constant mesh size of 50 mm, and the numerical results for SFEM and FEM are depicted in Fig. 5 and Table 1. Cases for which $\boldsymbol{kh} = 1$ and $\boldsymbol{k}^3\boldsymbol{h}^2 = 1$ are also presented in Fig. 5. It can be concluded that the relative errors at low wave numbers obtained from FEM and SFEM are both small. As wave number increases, the relative errors increase dramatically for both methods due to the $\boldsymbol{k}^3$ term, but the relative errors for SFEM solutions are smaller than those of FEM solutions.

Table 1
The relative error of function wave number $\boldsymbol{k}$.

Wave number ($\boldsymbol{k}$)	1	5	10	15	20	25
FEM (e)	0.00011	0.00292	0.06156	0.113103	0.29592	0.86688
SFEM (e)	0.00006	0.00169	0.02933	0.09674	0.28267	0.36006

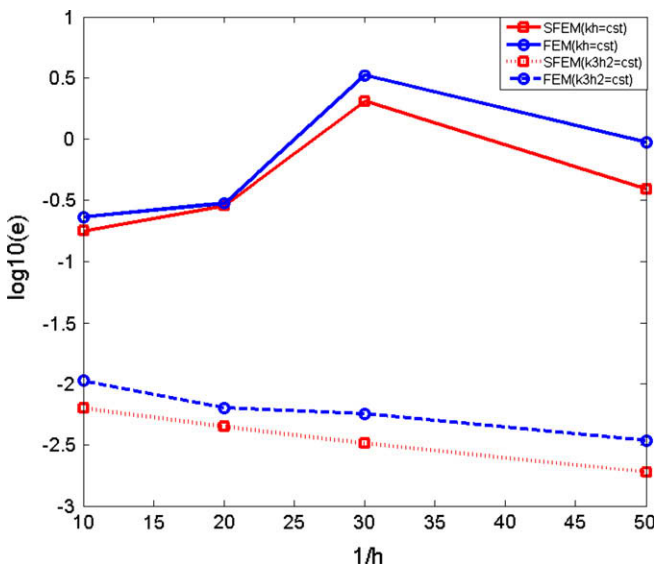

Fig. 6. Comparison of error obtained using the linear FEM and the SFEM.

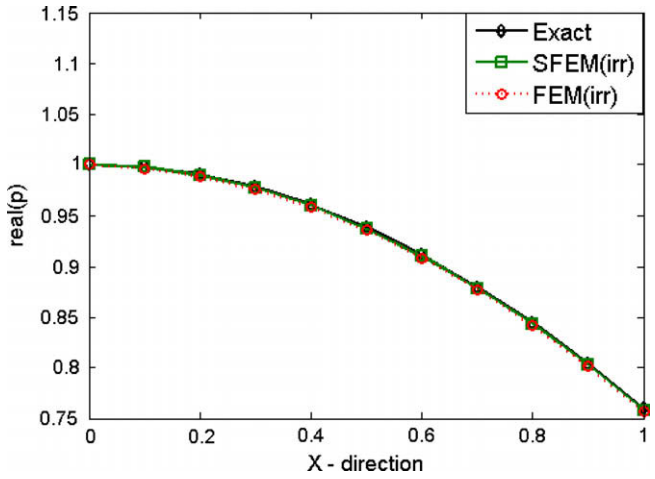

Fig. 7. Acoustic pressure distribution along the *x*-axis bottom boundary line at $\boldsymbol{k} = 1$.

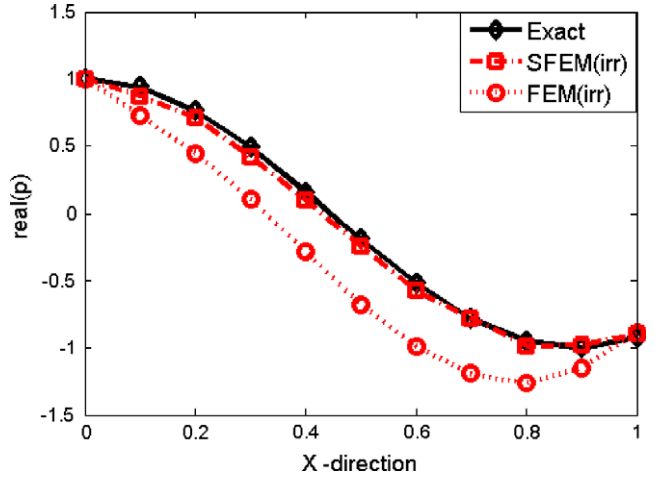

Fig. 8. Acoustic pressure distribution along the *x*-axis bottom boundary line at $\boldsymbol{k} = 5$.

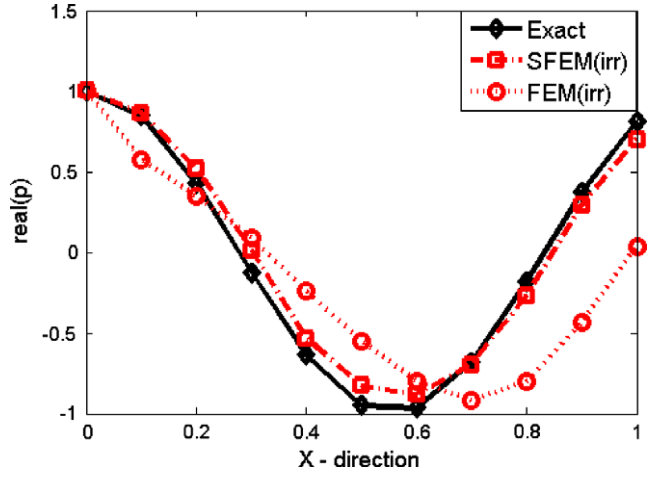

Fig. 9. Acoustic pressure distribution along the *x*-axis bottom boundary line at $\boldsymbol{k} = 8$.

4.4. Control of the pollution error

The pollution effect in the case of FEM was introduced in Section 4.1. Eq. (32) indicates that both $\boldsymbol{kh}$ and $\boldsymbol{k}^3\boldsymbol{h}^2$ must be considered to control the error. If the H^1 error is computed on a range of meshes with variable values of $\boldsymbol{h}$ while $\boldsymbol{kh}$ is kept constant, the upper bound of the error will increase linearly with $\boldsymbol{k}$. On the other hand, if $\boldsymbol{k}^3\boldsymbol{h}^2$ is kept constant, this error will be controlled. The results of this test for a two-dimensional problem (Section 4.2) are shown in Fig. 6. When keeping $\boldsymbol{kh}$ constant, the error in-

Table 2
Acoustic pressure of bottom boundary line using SFEM and FEM at $\boldsymbol{k} = 5$.

Field coordinate (m)	Exact solution (Re)	FEM		SFEM (SC = 3)	
		Pressure (Re)	*error* (Re) (%)	Pressure (Re)	*error* (Re) (%)
(0.2, 0.0)	0.7602	0.4496	40.8577	0.7113	6.4325
(0.4, 0.0)	0.1559	−0.2885	285.0545	0.0980	37.1392
(0.6, 0.0)	−0.5231	−0.9929	−89.8107	−0.5787	−10.6289
(0.8, 0.0)	−0.9514	−1.2631	−32.7622	−0.9869	−3.7313
(1.0, 0.0)	−0.9234	−0.8849	4.1694	−0.8986	2.6857

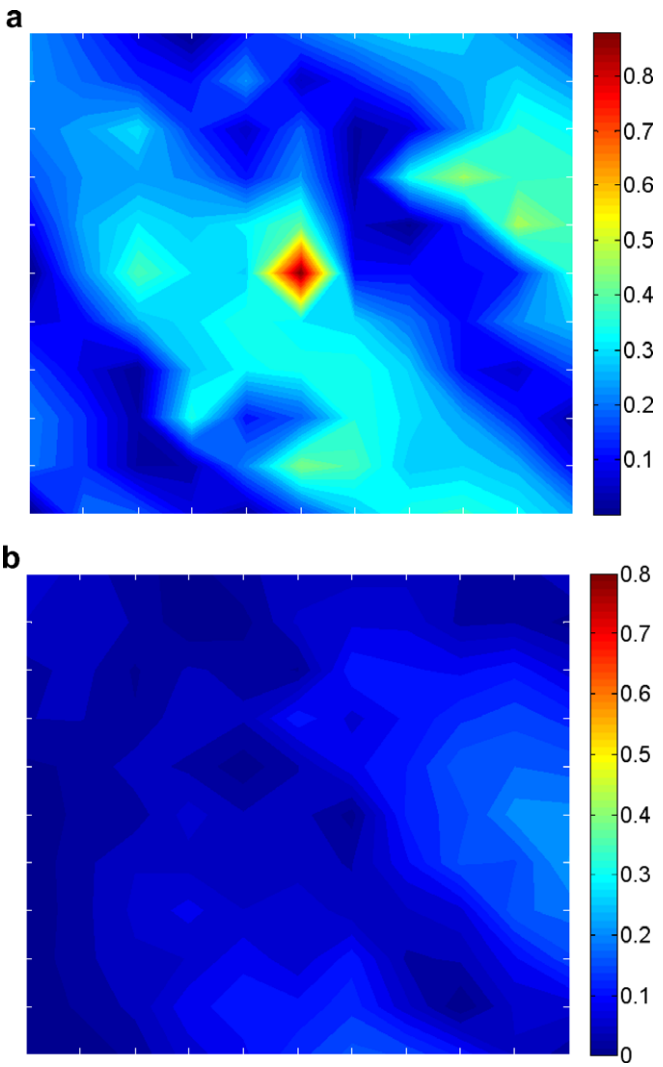

Fig. 10. Distribution of the error on Re(p): (a) using FEM and (b) using SFEM.

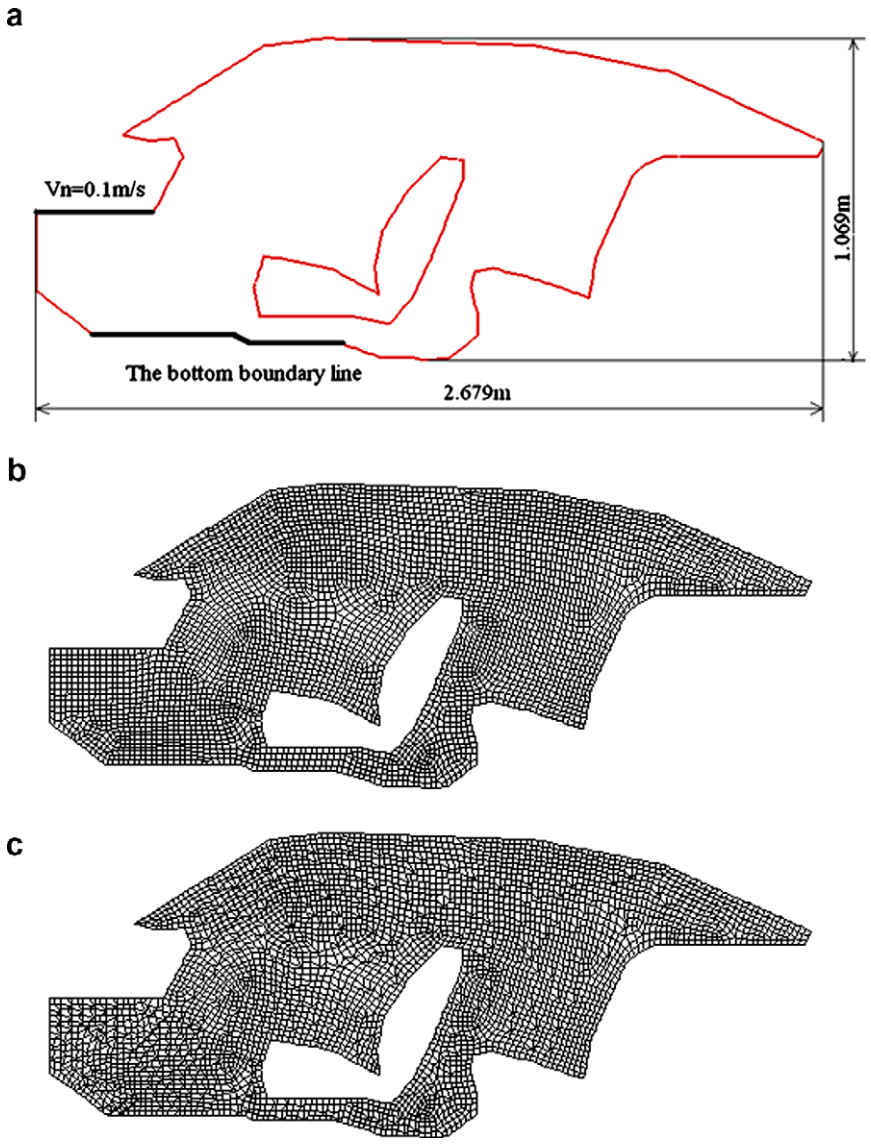

Fig. 11. (a) The model of 2D car interior cavity, (b) regular mesh, (c) irregular mesh.

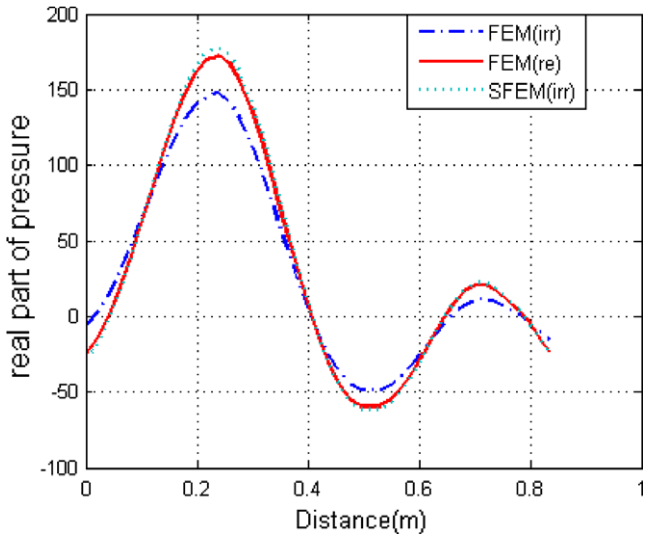

Fig. 12. Distribution of acoustic pressure along the defined bottom boundary line at $k = 15$.

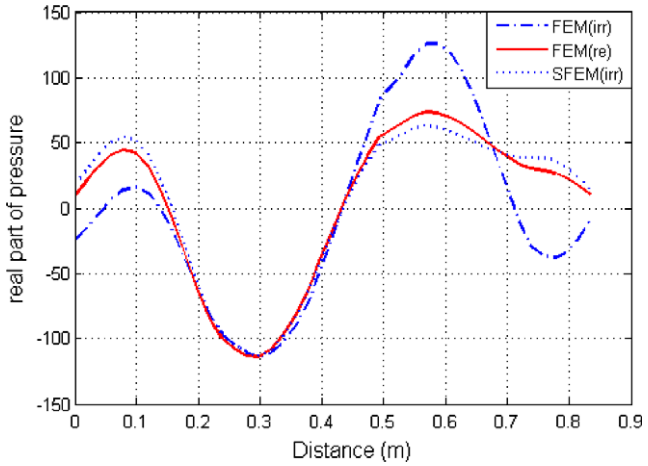

Fig. 13. Distribution of acoustic pressure along the defined bottom boundary line at $k = 20$.

creases linearly with $\boldsymbol{k} = 1/\boldsymbol{h}$ for the low values of $1/\boldsymbol{h}$ because most of the error is determined by the phase lag between the numerical and the exact solutions, which increases with $1/\boldsymbol{h}$. Once the phase shift is equal to one wavelength, the numerical wave coincides with the exact wave on a portion of Ω, giving a lower error although the solution is not more accurate. The graph also shows that keeping $\boldsymbol{k}^3\boldsymbol{h}^2$ constant controls the error.

A theoretical upper bound of the relative error in H^1 semi-norm equivalent to Eq. (32) has not yet been found for SFEM, but the same test was performed with SFEM, and the results are presented in Fig. 6. Fig. 6 demonstrates that the relative error in H' semi-norm in SFEM is slightly improved, as was the case in FEM, and must be controlled by keeping $\boldsymbol{k}^3\boldsymbol{h}^2$ constant; a criterion based on $\boldsymbol{kh}$ being constant does not seem to be sufficient, even if the accuracy is better with SFEM.

5. The effects of nodal irregularity

5.1. The effects of nodal irregularity for acoustic square domain

To evaluate the influence of mesh irregularities on accuracy, the acoustic square domain problem will be tested with regular mesh and irregular mesh. Two types of discretization were used, as shown in Fig. 2b and c, respectively. The irregularly distributed nodes are generated based on the degree of nodal irregularity defined by the following expression:

$$\begin{aligned} x' &= x + \Delta x \cdot r_c \cdot \alpha_{ir} \\ y' &= y + \Delta y \cdot r_c \cdot \alpha_{ir} \end{aligned} \tag{37}$$

where x' and y' are new coordinates for the interior node, x and y are the original coordinates, Δx and Δy are the initial regular element

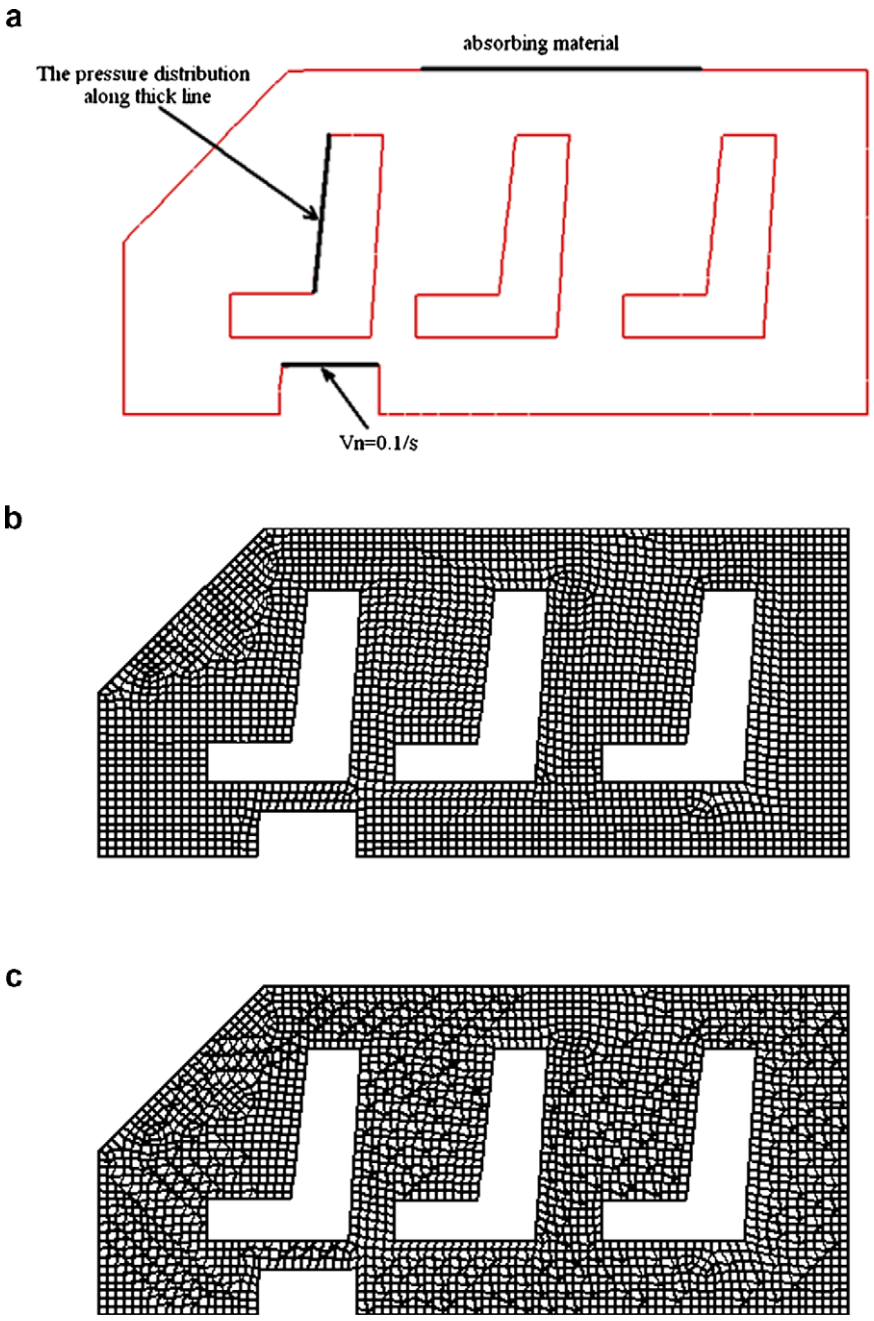

Fig. 14. (a) The model of 2D micro-car interior cavity with boundary condition, (b) regular mesh, (c) irregular mesh.

sizes in the x- and y-directions, respectively, r_c is a computer-generated random number between -1.0 and 1.0, and α_{ir} is a prescribed irregularity degree the value of which is varied between 0.0 and 0.5. The larger the value of α_{ir}, the more irregular the shape of the generated element becomes.

This test demonstrates the good characteristics of SFEM for the acoustic square domain with severely distorted elements. The study was performed at three different values of wave numbers ($\boldsymbol{k} = 1$, $\boldsymbol{k} = 5$, $\boldsymbol{k} = 8$) with two types of mesh. The acoustic pressure distributions computed using the ES-FEM along the x-axis are plotted in Figs. 7–9, together with the *exact* solution. For comparison, the FEM results are also presented in the figures. In these figures, the ***SFEM(irr)*** line denotes SFEM solutions with irregular mesh ($\alpha_{ir} = 0.5$); the ***SFEM(re)*** line denotes SFEM solutions with regular mesh ($\alpha_{ir} = 0.0$); the ***FEM(irr)*** line denotes FEM solutions with irregular mesh; and the ***FEM(re)*** line denotes FEM solutions with regular mesh. The pictures show that the FEM results become worse when irregular meshes are used, especially for the high wave number problem. The SFEM, however, is not sensitive to mesh distortions and wave number. These crucial findings imply that the present SFEM works well, even with extremely distorted elements.

The relative error norm in the real part of pressure is used to examine the computed results.

$$error\ (\mathrm{Re}) = \frac{real(p^{exact} - p^{h})}{real(p^{exact})} \tag{38}$$

Table 2 presents the real part of the numerical solutions along the x-axis boundary line. Both the FEM and SFEM solutions are presented with irregular arrangement elements for $\boldsymbol{k} = 5$. The distributions of absolute error $|real(p^{exact} - p^{k})|$ for FEM and SFEM are shown in Fig. 10a and b, respectively.

It can be observed from the figures and the table that: (1) the accuracy of FEM solutions is not stable and decreases with irregularly distorted elements; (2) the presented SFEM solutions have very little sensitivity to the distortion of the elements; and (3) the presented SFEM solutions have greater accuracy compared with linear FEM, even for the high wave numbers.

5.2. The effects of nodal irregularity for a 2D car acoustic problem

We now consider the problem of analyzing the acoustic pressure distribution with nodal irregularity in the passenger compartment of a car. The engine is the main source of noise in the passenger compartment. The geometry of the passenger compartment is approximately considered as prismatic, and it is possible to simplify it from three dimensions to two dimensions, as shown in Fig. 11a. The air density in the car cavity is 1.225 kg/m^3, and the speed at which sound travels in the air is 343 m/s. The panel of the passenger compartment is subjected to vibration coming from the engine at a velocity of 0.1 m/s. The roof of the passenger compartment does not contain any absorbent material to dampen the noise.

To investigate the effect of the shape of the quadrilateral element, we performed the same analysis as in Section 5.1. The passenger compartment was meshed using quadrilateral elements, and the regular and irregular meshes both had 4183 quadrilateral elements and 4487 nodes, as shown in Fig. 11b and c, respectively. Wave number values of 15 and 20 were studied in the irregular mesh model.

To show the quantitative results for these two wave number values, the real parts of the pressure obtained from SFEM (SC = 4) and FEM along the defined bottom boundary line shown in Fig. 11a are given in Figs. 12 and 13, respectively. Because an analytical solution is unavailable for this problem, a reference configuration using FEM with the regular mesh was used, and the results at wave number values of 15 and 20 are plotted in Figs. 12 and 13, respectively. The real parts of the pressure obtained from SFEM and FEM along the defined bottom boundary line are similar to the reference result at these wave numbers, but the results obtained from SFEM varied a little from the reference result, but the variance was much less than that of FEM, especially for high wave numbers. This numerical example validates that SFEM has obvious advantages of high accuracy when the meshes are severely distorted.

5.3. The effects of nodal irregularity for a 2D micro-car acoustic problem

In this subsection, we further consider a micro-car passenger compartment problem, as shown in Fig. 14a. Similar to the second example, the main source of noise in the micro-car compartment is the vibration of the engine. The floor panel of the passenger compartment is subject to the vibration that comes from the engine with a velocity of 0.1 m/s. The absorbing material is attached to the roof and the admittance is set at 0.002. The model is discretized with 2933 nodes, and the regular and irregular meshes are shown in Fig. 14b and c, respectively. The air density in the

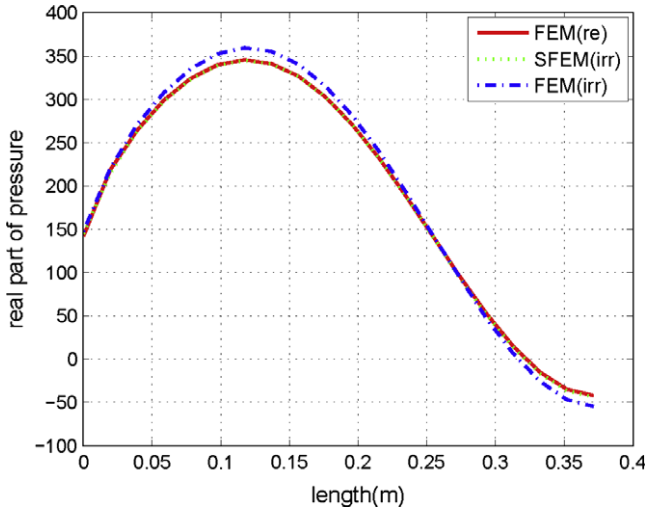

Fig. 15. Distribution of acoustic pressure along the defined thick line at $\boldsymbol{k} = 15$.

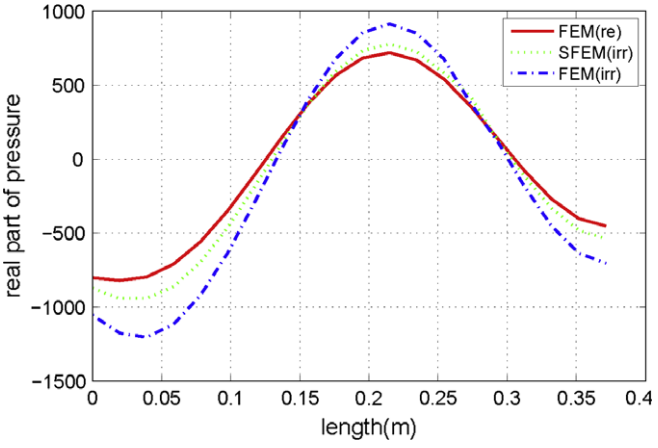

Fig. 16. Distribution of acoustic pressure along the defined thick line at $\boldsymbol{k} = 20$.

car cavity is 1.225 kg/m^3, and the speed at which sound travels through the air is 343 m/s. The wave number values of 15 and 20 were studied in the irregular mesh model. The real parts of the pressure obtained from SFEM (SC = 4) and FEM along the defined thick line shown in Fig. 14a are given in Figs. 15 and 16, respectively. It is observed that SFEM gives results that are comparable to FEM for the severely distorted meshes, especially for high wave number problems.

6. Conclusions

In this work, SFEM was further formulated for obtaining numerical solutions for 2D acoustic problems. The smoothed Galerkin weak form was used to formulate the discretized system equations, and the cell-wise acoustic gradient smoothing technique was introduced. An acoustic square domain problem was investigated in detail to study the accuracy, convergence, and error control of SFEM. Some acoustic problems were investigated to evaluate the influence of mesh irregularities on accuracy, and the following conclusions resulted from the work:

(1) The SFEM performs a smoothing operation on the acoustic gradient matrix, and the smoothed acoustic stiffness matrix was easily obtained; no additional parameters or degrees of freedom were needed, and the method can be implemented in a straightforward way with little change to the FEM code.
(2) The SFEM achieves higher efficiency and accuracy and is not sensitive to mesh distortions compared to FEM, especially for high wave number problems.
(3) Due to the low demand of mesh quality and limited manpower requirements in pre-processing, SFEM has great potential for use in the practical analysis of acoustic problems.

Acknowledgement

This work was supported by Program for Changjiang Scholar and Innovative Research Team in University (5311050050037) and the Science Fund of State Key Laboratory of Advanced Design and Manufacturing for Vehicle Body No.60870002 and No.60870005.

References

[1] Ihlenburg F, Babuska I. Dispersion analysis and error estimation of Galerkin finite element methods for the Helmholtz equation. Int J Numer Methods Eng 1995;38:3745–74.
[2] Bales L, Lasiecka I. Continuous finite elements in space and time for the nonhomogeneous wave equation. Comput Math Appl 1994;27:91–102.
[3] French DA, Peterson TE. A continuous space–time finite element method for the wave equation. Math Comput 1996;65:49–1506.
[4] Bouillard Ph, Ihlenburg F. Error estimation and adaptivity for the finite element method in acoustics: 2D and 3D applications. Comput Methods Appl Mech Eng 1999;176:147–63.
[5] Wu S-W, Lian S-H, Hsu L-H. A finite element model for acoustic radiation. J Sound Vib 1998;215:489–98.
[6] Chen JT, Chen KH, Chyuan SW. Numerical experiments for acoustic modes of a square cavity using the dual boundary element method. Appl Acoust 1999;57:293–325.
[7] Harari Isaac, Magoules Frederic. Numerical investigations of stabilized finite element computations for acoustics. Wave Motion 2004;39:339–49.
[8] Petersen Steffen, Dreyer Daniel, Estorff Otto von. Assessment of finite and spectral element shape functions or efficient iterative simulations of interior acoustics. Comput Methods Appl Mech Eng 2006;195:6463–78.
[9] Bouillard Ph. Admissible fields and error estimation for acoustic FEA with low wavenumbers. Comput Struct 1999;73:227–37.
[10] Bouillard Ph, Suleau S. Element-Free Galerkin solutions for Helmholtz problems: formulation and numerical assessment of the pollution effect. Comput Methods Appl Mech Eng 1998;162:317–35.
[11] Bouillard Ph, Lacroix V, De Bel E. A wave-oriented meshless formulation for acoustical and vibro-acoustical applications. Wave Motion 2004;39:295–305.
[12] Kireeva O, Mertens T, Bouillard Ph. A coupled EFGM–CIE method for acoustic radiation. Comput Struct 2006;84:2092–9.
[13] Liu GR, Nguyen TT, Dai KY, Lam KY. Theoretical aspects of the smoothed finite element method (SFEM). Int J Numer Methods Eng 2007;71:902–30.
[14] Liu GR, Dai KY, Nguyen TT. A smoothed finite element method for mechanics problems. Comput Mech 2007;39:859–77.
[15] Nguyen-Xuan H, Rabczuk T , Bordas S, Debongnie JF. A smoothed finite element method for plate analysis. Comput Methods Appl Mech Eng 2008;197:1184–203.
[16] Nguyen-Thanh N, Rabczuk Timon, Nguyen-Xuan H, Bordas Stéphane PA. A smoothed finite element method for shell analysis. Comput Methods Appl Mech Eng 2008;198:165–77.
[17] Cui XY, Liu GR, Li GY, Zhao X, Nguyen TT, Sun GY. A smoothed finite element method (SFEM) for linear and geometrically nonlinear analysis of plates and shells. Comput Model Eng Sci 2008;28:109–25.
[18] Dai KY, Liu GR. Free and forced vibration analysis using the smoothed finite element method (SFEM). J Sound Vib 2007;301:803–20.
[19] Ihlenburg F, Babuska I. Finite element solution of the Helmholtz equation with high wave number. Part 1: The *h*-version of the FEM. Comput Math Appl 1995;38(9):9–37.
[20] Ihlenburg F, Babuska I. Finite element solution of the Helmholtz equation with high wave number. Part 2: The hp-version of the FEM. SIAM J Numer Anal 1997;34(l):315–58.
[21] Ihlenburg F, Babuska I. Reliability of finite element methods for the numerical computation of waves. Adv Eng Software 1997;28:417–24.